Seventh International Conference on Computational Fluid Dynamics (ICCFD7), Big Island, Hawaii, July 9-13, 2012 **ICCFD7-4204**

Multi-dimensional Limiting Strategy for Arbitrary Higher-order Discontinuous Galerkin Methods in Inviscid and Viscous Flows

J. S. Park* and C. Kim*
Corresponding author: chongam@snu.ac.kr

* Seoul National University, Korea.

Abstract: The present paper deals with the multi-dimensional limiting process (MLP) for arbitrary higher-order discontinuous Galerkin (DG) methods to compute compressible inviscid and viscous flows. MLP, which has been quite successful in finite volume methods (FVM), is extended into DG methods for hyperbolic conservation laws. From the previous works, it was observed that the MLP methods provide an accurate, robust and efficient oscillation-control mechanism in multiple dimensions for linear reconstruction. This limiting philosophy can be extended into higher-order reconstruction. The proposed algorithm, called the hierarchical MLP, facilitates the accurate capturing of detailed flow structures in both continuous and discontinuous regions. Through extensive numerical analyses and computations on triangular and tetrahedral grids, it is demonstrated that the proposed limiting approach yields the desired accuracy and outstanding performances in resolving compressible inviscid and viscous flow features.

Keywords: Higher-order Methods, Multi-dimensional Limiting Process, Arbitrary Higher-order DG Methods, Inviscid and Viscous Flows.

1 Introduction

Up to now, second-order accurate flow solvers with a discontinuity capturing strategy are widely used to resolve compressible viscous flows. At the same time, they also yield some limitations, particularly in capturing unsteady vortex-dominated flow structures due to excessive numerical diffusion. By improving the accuracy of spatial and temporal discretization, higher-order CFD methods can provide the detailed flow structure with reasonable computational resource [1, 2]. Among them, the discontinuous Galerkin (DG) methods have become popular as a higher-order discretization of hyperbolic conservation laws owing to its distinctive merits, such as flexibility to handle complex geometry, compact stencil for higher-order reconstruction, and amenability to parallelization and *hp*-refinement. This method has been applied to convection problem, high order partial differential equation (PDE), such as elliptic-type PDE or the Navier-Stokes equations. Recent studies show some encouraging results to resolve compressible turbulent flows by the DG methods [3].

A few issues, however, have been blamed as obstacles in extending the DG methods (or higher-order methods in general) into high speed unsteady flows. One of them is to design a robust, accurate and efficient limiting algorithm to suppress unwanted oscillations around discontinuities without compromising the higher-order nature of the DG discretizations. Various limiting algorithms, such as slope limiter [4], moment limiter [5, 6, 7], hierarchical reconstruction [8, 9] and ENO/WENO type limiter [10, 11, 12] have been combined with the DG methods. These approaches have been successful in some parts, but overall performances indicate further elaboration is definitely necessary, particularly in controlling oscillations near shock discontinuities in multi-dimensional flows. In addition, most of the above-mentioned approaches require characteristic variable decomposition at the limiting stage which may degrade solution accuracy due to misidentification of the troubled-cells. Implementation procedure is rather complicated with a delicate tuning of several parameters, and the required limiting stencil becomes wider for higher than DG-*P3* reconstruction.

The fundamental cause of such problems essentially lies in the framework of mathematical analyses based on the one-dimensional convection equation, which in general do not guarantee multi-dimensional monotonicity. Recently, the multi-dimensional limiting process (MLP), with the theoretical foundation of the maximum principle, has been successfully proposed in the finite volume framework (FVM). Compared with traditional limiting strategies, such as the TVD or ENO-type limiting, the MLP limiting efficiently controls unwanted oscillations particularly in multi-dimensional flow situations. By imposing the MLP condition on both cell-centered and cell-vertex values, the MLP limiting can efficiently follow the multi-dimensional flow physics, which leads to the global/local L^∞ stability. A series of previous researches [13, 14, 15] demonstrated that the MLP limiting possesses superior characteristics in terms of accuracy, robustness and efficiency in inviscid and viscous computations on structured and unstructured grids within the FVM framework.

Based on its remarkable progresses in FVM, the MLP limiting philosophy is extended into the DG framework to provide an accurate, efficient and robust limiting method for higher-order discretizations. As a way to stabilize the higher-order DG reconstruction, the original MLP condition is extended to take into account the behavior of local extrema produced by a cell-wise higher-order interpolation. As a result, the augmented MLP condition and the MLP-based troubled-cell marker are obtained, which pave the way to obtain the hierarchical MLP formulation up to arbitrary order of DG-*Pn* reconstruction. The hierarchical MLP method developed for inviscid compressible flows [16, 17] is now extended for viscous compressible flows. To handle the second-order derivative terms, such as viscous stress or heat flux, the BR2 method [18] is applied. The present work provides the computed results up to DG-*P3* reconstruction on triangular and tetrahedral grids. Since the proposed limiting algorithm relies only on the MLP stencil regardless of the order of reconstruction, it facilitates an easy extension to arbitrary higher-order DG reconstruction.

The present work is organized as follows. At first, the baseline discretization methods are briefly summarized in Section 2. Then, the hierarchical MLP limiting procedure is described in Section 3. In Section 4, extensive numerical experiments are carried out to verify the favorable properties of the proposed limiting strategy for inviscid and viscous compressible flows. Finally, conclusion will be given in Section 5.

2 Discontinuous Galerkin Methods

In order to analyze the inviscid and viscous compressible flows, the Euler and Navier-Stokes equations are considered.

$$\frac{\partial \mathbf{Q}}{\partial t} + \nabla \cdot (\mathbf{F}_c - \mathbf{F}_v) = 0, \tag{1}$$

where $\mathbf{Q}$ is the conservative variable vector, $\mathbf{F}_c$ and $\mathbf{F}_v$ are the inviscid and viscous flux.

Discretization using the DG methods starts from the weak form of Eq. (1) on the cell T_j.

$$\int_{T_j} \frac{\partial \mathbf{Q}}{\partial t}\mathbf{W} dV + \int_{\partial T_j} (\mathbf{F}_c - \mathbf{F}_v)\cdot \mathbf{n}\mathbf{W} dS - \int_{T_j} (\mathbf{F}_c - \mathbf{F}_v)\nabla \mathbf{W} dV = 0, \tag{2}$$

where $\mathbf{W}$ is a test function vector, and $\mathbf{n}$ is the outward unit normal vector.

Distribution within a cell is then approximated by the sum of shape functions in a suitably smooth function space V^n, which usually consists of polynomials of order up to n. The test function is also approximated in the same function space V^n.

$$\mathbf{Q}_j^h(\mathbf{x}, t) = \sum_{i=1}^{n} \mathbf{Q}_j^{(i)}(t) b_j^{(i)}(\mathbf{x}), \tag{3}$$

where $\mathbf{Q}_j^h$ is an approximated state variable vector on the cell T_j. $b_j^{(i)}$ is a shape function, which is a local orthogonal shape function in the present work.

After applying suitable numerical fluxes, the approximated solution in V^n on the cell T_j can be written

Table 1: Quadrature points for boundary and domain integration.

	Triangular element			Tetrahedral element		
	P1	*P2*	*P3*	*P1*	*P2*	*P3*
Boundary	2	3	4	4	7	13
Domain	3	7	12	4	11	24

as follows.

$$\int_{T_j} \frac{\partial \mathbf{Q}_j^h}{\partial t} \mathbf{B}_j dV + \int_{\partial T_j} \mathbf{H}_c \left(\mathbf{Q}_{jk}^h, \mathbf{Q}_{kj}^h\right) \cdot \mathbf{n} \mathbf{B}_j dS - \int_{T_j} \mathbf{F}_c \left(\mathbf{Q}_j^h\right) \cdot \nabla_h \mathbf{B}_j dV$$
$$- \int_{\partial T_j} \mathbf{H}_v \left(\mathbf{Q}_{jk}^h, \mathbf{\Theta}_{jk}^h, \mathbf{Q}_{kj}^h, \mathbf{\Theta}_{kj}^h\right) + \int_{T_j} \mathbf{F}_v \left(\mathbf{Q}_j^h, \mathbf{\Theta}_j^h\right) \cdot \nabla_h \mathbf{B}_j dV = 0, \tag{4}$$

where $\mathbf{Q}_{jk}^h$ is the cell interface state vector in the direction from T_j to its neighboring cell T_k, and $\mathbf{B}_j$ is the vector of the basis functions. $\mathbf{H}_c\left(\mathbf{Q}_L, \mathbf{Q}_R\right)$ and $\mathbf{H}_v\left(\mathbf{Q}_L, \mathbf{\Theta}_L, \mathbf{Q}_R, \mathbf{\Theta}_R\right)$ are the tensors of a numerical inviscid and viscous flux function.

To handle the second-order derivative terms in viscous stress and heat flux, auxiliary variable vector is introduced as follows.

$$\Theta - \nabla \mathbf{Q} = 0 \tag{5}$$

From the BR2 scheme, Eq. (5) can be discretized by introducing the lift operator.

$$\mathbf{\Theta}_{jk}^h = \nabla_h \mathbf{Q}_{jk}^h + \eta \mathbf{r}_e([\mathbf{Q}^h]), \quad \mathbf{\Theta}_j^h = \nabla_h \mathbf{Q}_j^h + \mathbf{r}([\mathbf{Q}^h]). \tag{6}$$

Plugging Eq. (6) into Eq. (4), the primal formulation of the governing equation can be obtained. The detailed derivation to treat the diffusion flux can be founded on Ref. [18]. The boundary and domain integration can be performed by exact formulation or numerical integration with polynomials of order of up to $2n$ and $2n{+}1$, respectively. The present computations adopt the Guass quadrature rule that is summarized in Table. 1.

Contrary to FVM, DG methods can realize arbitrary higher-order reconstructions within compact stencil. At the same time, however, DG formulation can be unstable especially in computing discontinuous solutions. The present approach is based on the RKDG method to overcome the stability problem [4], which is composed of two key ingredients: one is a stable time integration scheme, and the other is a robust limiting procedure. The present study focuses on the limiting issue, which is going to be elaborated in the following section. For the time integration, nonlinear stable methods are applied, such as the third-order accurate TVD Runge-Kutta method or the five-stage fourth-order accurate strong stability preserving Runge-Kutta method (SSPRK(5,4)) [19]. The time step limitation for explicit DG methods are severe, especially due to the diffusion term [20, 21]. In the present computations, we use the following definition of time step.

$$\Delta t = \frac{CFL}{2n+1} \frac{h}{|\lambda_c^{\max}| + d|\lambda_v^{\max}|\frac{2n+1}{h}}, \tag{7}$$

where d is the number of dimension and h is the radius of inscribed circle or sphere for triangular and tetrahedral element, respectively. $\lambda_c^{\max}$ and $\lambda_v^{\max}$ is the maximum wave speed of inviscid and viscous flux, respectively. Courant number has been set to 0.9 for DG-*P1* or *P2* with TVD Runge-Kutta method and 1.4 for DG-*P3* with SSPRK(5,4).

3 Multi-dimensional Limiting Strategy for DG Reconstruction

Limiting should be activated only on the troubled-cells to maintain higher-order accuracy across smooth extrema. An accurate troubled-cell marker, followed by a sophisticated limiting, is thus crucial to obtain an accurate monotone profile in the DG framework. Some troubled-cell markers, such as the TVB marker [4] or KXRCF marker [22], have been developed and combined with slope limiters or WENO-type limiters, but the precise detection of the troubled-cells is not an easy task. We propose a new indicator based on the MLP concept to detect the troubled-cells. For the troubled-cells, MLP-u slope limiters, which were successfully developed in finite volume methods, are applied. At first, we briefly summarize MLP-u slope limiters and describe the implementation procedure for higher-order DG reconstruction.

3.1 MLP-u Slope Limiter

In order to enforce multi-dimensional monotonicity, the MLP condition has been proposed in the finite volume methods. This condition is an extension of the one-dimensional monotonicity condition, by considering the case where the direction of local flow gradient is not aligned to the local grid line. The starting point of the MLP condition is that local extrema always occur at vertex point if property distribution is linear. It manifests that i) treatment of vertex point is essential in limiting stage, ii) all information around vertex point should be incorporated to avoid multi-dimensional oscillations, which leads to the following MLP condition.

$$\bar{q}_{v_i}^{\min} \leq q_{v_i} \leq \bar{q}_{v_i}^{\max}, \tag{8}$$

where q_{v_i} is the value at v_i, and $(\bar{q}_{v_i}^{\min}, \bar{q}_{v_i}^{\max})$ are the minimum and maximum cell-averaged values among all the cells sharing v_i. Equation (8) is required to be satisfied at both cell-centered and vertex points. It is noted that the MLP condition can be applied to any type of mesh since it does not assume a particular mesh connectivity. At the same time, it is also observed that well-controlled vertex value at interpolation/limiting stage makes it possible to produce monotonic distribution of cell-averaged values. Extensive numerical experiments [13, 14, 15] strongly support that full realization of Eq. (8) is very effective to preserve accurate monotone profiles.

This philosophy can be readily extended on unstructured grids with second-order accurate reconstruction. Sub-cell interpolation may start from the unstructured version of the MUSCL-type linear reconstruction as follows.

$$q_j(r) = \bar{q}_j + \phi \nabla \bar{q}_j \cdot \mathbf{r}, \tag{9}$$

where q is the the state variable, $\nabla \bar{q}_j$ is the gradient within the cell T_j, and $\mathbf{r}$ is the position vector from the centroid of T_j. ϕ is a function to be designed by limiting strategy. After applying the MLP condition to vertex point, the MLP slope limiter is introduced to ensure multi-dimensional monotonicity by considering all the distributions around the common vertex v_i. The range of the MLP slope limiting is then obtained as follows.

$$0 \leq \phi \leq \max\left(\frac{\bar{q}_{v_i}^{\min} - \bar{q}}{\nabla \bar{q} \cdot \mathbf{r}_{v_i}}, \frac{\bar{q}_{v_i}^{\max} - \bar{q}}{\nabla \bar{q} \cdot \mathbf{r}_{v_i}} \right). \tag{10}$$

From Eq. (10), the MLP-u slope limiters can be obtained as follows.

$$\phi_{MLP} = \min_{\forall v_i \in T_j} \left\{ \begin{array}{ll} \Phi(r_{v_i,j}) & \text{if } \nabla \bar{q}_j \cdot \mathbf{r}_{v_i,j} \neq 0 \\ 1 & \text{otherwise} \end{array} \right. , \tag{11}$$

where $r_{v_i,j} = (\bar{q}_{v_i}^{\min \ or \ \max} - \bar{q}_j)/\nabla \bar{q}_j \cdot \mathbf{r}_{v_i,j}$ is the ratio of the minimum or maximum allowable variation to the estimated variation at v_i of T_j. $\mathbf{r}_{v_i,j}$ is the position vector from the centroid of T_j to the vertex v_i. By determining $\Phi(r)$ to satisfy the maximum principle, we have the MLP-u1 and MLP-u2 limiters. Detailed implementation in unsteady and steady flows can be found in Refs. [14, 15].

The MLP limiting is supported by the maximum principle in ensuring the monotonicity in multiple dimensions. For multi-dimensional scalar conservation law, the MLP limiting guarantees the following local maximum principle under a suitable CFL condition [14, 15].

$$\text{If } \ \bar{q}_{j,neighbor}^{\min,n} \leq \bar{q}_j^n \leq \bar{q}_{j,neighbor}^{\max,n}, \ \text{ then } \ \bar{q}_{j,neighbor}^{\min,n} \leq \bar{q}_j^{n+1} \leq \bar{q}_{j,neighbor}^{\max,n}. \tag{12}$$

Here, $\bar{q}_j$ is the cell-averaged value on T_j, and $(\bar{q}_{j,neighbor}^{\min,n}, \bar{q}_{j,neighbor}^{\max,n})$ are the minimum and maximum cell-averaged values on the MLP stencil. The MLP stencil is defined as the union of the cells sharing an edge or vertex of the cell T_j. In conjunction with the MLP condition (Eq. (8)), Eq. (12) simply states that the MLP limiting satisfies the MLP condition at cell-centered point at every time step.

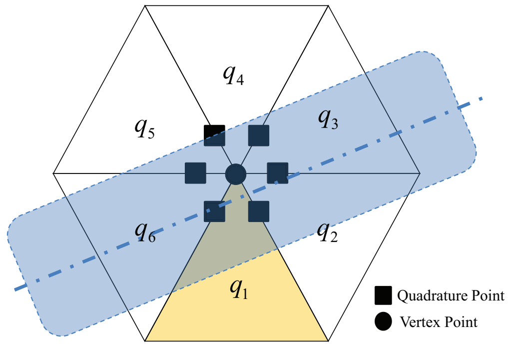

Figure 1: Discontinuity on the MLP stencil. (Dash-dot line is a discontinuity and spurious oscillations may occur in the blue-shaded region.)

The MLP condition on the MLP stencil makes it realizable to capture multi-dimensional flow structure accurately while maintaining the required order-of-accuracy. From Eqs. (8) and (12), the updated solution by the MLP limiting satisfies the maximum principle both on cell-centered and cell-vertex points, though the stencil involved is a bit different. In addition, from the global/local L^∞ stability of computed solutions, the MLP limiting satisfies the LED condition in a truly multi-dimensional way [15].

3.2 Augmented MLP Condition

The MLP condition in FVM is used to identify and control the maximum-principle-violating cells [14, 15]. If property distribution is linear, the edge/face midpoint (or any quadrature point) must be restricted through controlling the vertex points where extrema occur. For higher-order reconstruction greater than *P1*, however, such privilege is no longer endowed. Since the *P1*-based MLP condition may omit some troubled-cells violating the maximum principle, additional condition should be imposed on the troubled-cell marker which can hold for arbitrary order of reconstruction.

In general, a higher-order DG reconstruction in a cell affects the higher-order distributions of the adjacent cells through the dynamic interaction occurring at the steps of flux evaluation and solution update. If we have a discontinuity near the vertex, as shown in Fig. 1, the higher-order DG reconstruction would trigger unwanted oscillations in the blue-shaded region. For *P1* reconstruction, any quadrature point in the cell can be readily controlled since its physical value is always bounded by the vertex values estimated from the linear reconstruction in the cell. For greater than *P1* reconstruction, we may have the quadrature points whose property values are no longer bounded by the vertex values. They can be outside the range imposed by the MLP condition (Eq. (8)) and thus have the danger of violating the maximum principle (Eq. (12)). Furthermore, it may happen even if the vertex value does satisfy the MLP condition. This suggests that the MLP condition reflecting a single sub-cell distribution only no longer holds, and all the higher-order DG distributions of the adjacent cells need to be checked even if we want to control quadrature points in the single cell. For example, as a way to control distribution along the boundary including such suspicious quadrature points, all the cells sharing the common vertex (q_1 to q_6 cells in Fig 1) are examined even if one of the MLP stencil (q_1 cell) is to be limited. From this perspective, we propose a more strict condition, called the augmented MLP condition, as follows. The augmented MLP condition is then used as the MLP-based troubled-cell marker for higher-order reconstruction.

$$\bar{q}_{v_i}^{\min} \leq q_{v_i}^{h,\min} \leq q_{v_i}^{h}, \quad q_{v_i}^{h} \leq q_{v_i}^{h,\max} \leq \bar{q}_{v_i}^{\max}, \tag{13}$$

where $q_{v_i}^h$ is an interpolated value at vertex v_i and $(q_{v_i}^{h,\min}, q_{v_i}^{h,\max})$ are the minimum and maximum interpolated values at v_i among all the cells sharing v_i. If any of the estimated vertex values violates the above condition, it is tagged as a troubled-cell. Numerical experiments strongly support that the MLP slope limiter with the augmented MLP condition is quite successful in handling multi-dimensional oscillations.

Similar to the MLP condition, the augmented MLP condition itself does not provide any mechanism to distinguish local extrema. In order to preserve the accuracy across smooth extrema, a simple but effective

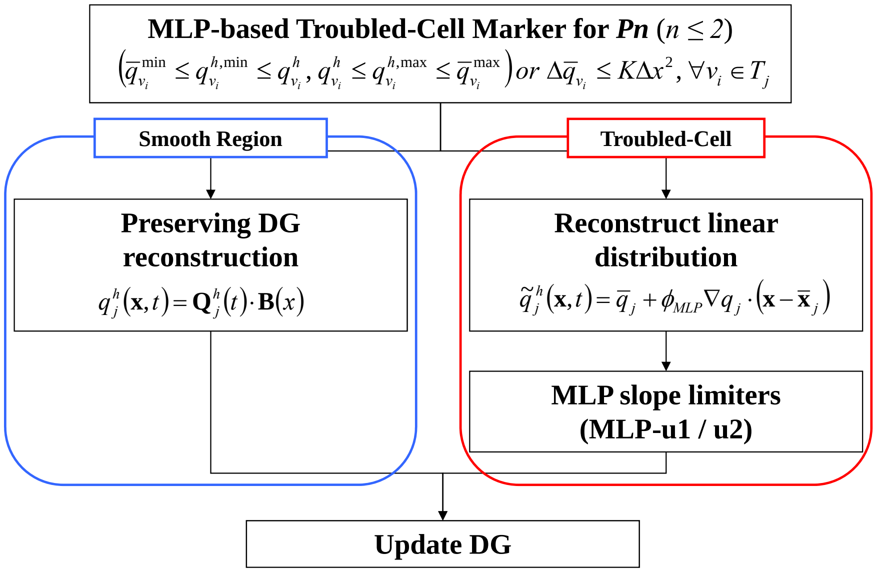

Figure 2: Flowchart of the MLP limiting procedure up to DG-*P2* reconstruction.

extrema detector is introduced as follows.

$$\Delta\bar{q}_{v_i} = \bar{q}_{v_i}^{\max} - \bar{q}_{v_i}^{\min} \le K\Delta x^2, \tag{14}$$

where K is a parameter to be determined.

The augmented MLP condition (Eq. (13)) together with the simple extrema detector (Eq. (14)) leads to a MLP-based troubled-cell marker. By combining the troubled-cell marker and the MLP-u slope limiters (Eq. (11), see [14, 15] for details), the MLP limiting strategy up to *P2* reconstruction is obtained. If a cell is tagged as a troubled cell, the *P2* distribution is projected onto the linear function space V^1. For the orthogonal shape function, this is accomplished by simply neglecting the *P2* mode. The MLP-u slope limiter developed in FVM is then applied to the linear distribution. Figure 2 shows the schematic summary of the MLP limiting procedure up to DG-*P2* reconstruction.

3.3 Hierarchical MLP limiting for DG-*Pn* reconstruction (n $\ge$ 2)

The MLP-based troubled-cell marker given by the augmented MLP condition and the simple extrema detector yields quite successful performances to control multi-dimensional oscillations. In fact, the augmented MLP condition can be extended into general DG-*Pn* reconstruction as an accurate troubled-cell marker. However, the problem to determine the optimal value of K for smooth extrema still remains. More seriously, the optimal value of K may change depending on the order of reconstruction. Thus, the simple extrema detector is not further employed. Instead, a hierarchical extrema detector for arbitrary DG-*Pn* reconstruction is deduced by examining the behavior of local extrema around vertex point.

Firstly, we decompose DG-*Pn* reconstruction into the sum of linear part (*Pn*-projected slope) and higher-order part (*P1*-filtered *Pn*), as follows.

$$q_{v_i,j}^{h,Pn} = \bar{q}_j + \underbrace{(L-\bar{q}_j)}_{Pn\text{-projected slope}} + \underbrace{\left(q_{v_i,j}^{h,Pn} - L\right)}_{P1\text{-filtered } Pn}, \tag{15}$$

where $q_{v_i,j}^{h,Pn}$ is the interpolated value at v_i obtained by Pn reconstruction on the cell T_j. L indicates the projection of Pn reconstruction on the $P1$ space. If we employ the local orthogonal shape function, L can be obtained by simply neglecting the higher-order term, *i.e.*, $L = q_{v_i}^{h,P1}$. The linear part simply represents the averaged slope for Pn reconstruction. From the mean value theorem, if local extrema appear around the vertex v_i, the gradient direction of $q^{h,Pn}_{v_i,j}$ would be substantially different from that of the linear part. If one goes up, the other would go down. Even if they are in the same direction, the magnitude of the gradient of $q^{h,Pn}_{v_i,j}$ would be smaller than that of the linear part. From the above observation, we can deduce the following extrema detector for local extrema around the vertex v_i.

- C1) If there is a local maximum around the vertex v_i,

  Pn-projected slope > 0, $P1$-filtered $Pn < 0, q^{h,Pn}_{v_i,j} > \bar{q}^{\min}_{v_i}$
- C2) If there is a local minimum around the vertex v_i,

  Pn-projected slope < 0, $P1$-filtered $Pn > 0, q^{h,Pn}_{v_i,j} < \bar{q}^{\max}_{v_i}$ (16)

The last inequalities ($q^{h,Pn}_{v_i,j} > \bar{q}^{\min}_{v_i}$, $q^{h,Pn}_{v_i,j} < \bar{q}^{\max}_{v_i}$) are necessary to treat stiff gradients including physical discontinuities. In addition, we add the following deactivation condition to avoid almost constant region.

$$\left| \frac{q^{h,Pn}_{v_i,j} - \bar{q}_j}{\bar{q}_j} \right| \leq 0.001 \tag{17}$$

By combining the augmented MLP condition (Eq. (13)) and the extrema detector (Eq. (16)), we formulate the hierarchical MLP limiting, which extends the simple MLP-based limiting strategy into arbitrary DG-Pn reconstruction. The limiting procedure higher than $P2$ reconstruction can be written as follows.

$$\begin{aligned}
q^{h,p2}_j &= \bar{q}_j + \phi_{MLP-u}(P1_j) + \varphi^{P2}\left(P2_j\right), \\
q^{h,P3}_j &= \bar{q}_j + \phi_{MLP-u}(P1_j) + \varphi^{P2}\left(P2_j + \varphi^{P3}(P3_j)\right), \\
&\ldots \\
q^{h,Pn}_j &= \bar{q}_j + \phi_{MLP-u}(P1_j) + \varphi^{P2}\left(P2_j + \varphi^{P3}(P3_j + \varphi^{P4}(\ldots + \varphi^{Pn}Pn_j)))\right).
\end{aligned} \tag{18}$$

Here, Pn_j is the $n-th$ order term that is orthogonal to V^{n-1} space on the cell T_j. If the orthogonal shape function is employed, it is simply the sum of the $n-th$ order shape modes on T_j. φ^{Pn} is the MLP troubled-cell marker for Pn reconstruction, which is formulated as follows.

$$\varphi^{Pn} = \min_{\forall v_i \in T_j} (\psi^{Pn}_{v_i,j}) \tag{19}$$

$\psi^{Pn}_{v_i,j}$ takes the value of 1 or 0 depending on the results of the augmented MLP condition (Eq. (13) and the extrema detector (Eqs. (16), (17)). If Eq. (13) is not satisfied, the extrema detector is employed to check local smoothness. If Eq. (16) and Eq. (17) are not satisfied, $\psi^{Pn}_{v_i,j}$ becomes 0. Otherwise, $\psi^{Pn}_{v_i,j} = 1$. After probing all vertex points, the final limiting function is determined as Eq. (19). The limiting procedure of Eq. (18) can be applied in a hierarchical manner from the highest mode to the lowest $P2$ mode. At first, the troubled-cell marker is applied to the highest order reconstruction. If the cell is tagged as a normal cell, the highest order term is kept unlimited. If not, Pn_j is ignored and the whole reconstruction is projected on V^{n-1} space to obtain the $P1_j$ to $P(n-1)_j$ modes. It can be done by simply moving onto $P(n-1)_j$ if the orthogonal shape functions are employed. This procedure is carried out recursively until the $P2$ reconstruction. If the $P2_j$ mode has to be limited, the linear term is computed by the MLP-u slope limiters developed in FVM. Figure 3 shows the schematic summary of the hierarchical DG-MLP limiting procedure.

The performance of the MLP troubled-cell marker is examined by checking the activation region with the following two-dimensional profiles. This is the multi-dimensional extension of the benchmark test for one-dimensional troubled-cell marker [7].

$$q_0 = \begin{cases} G(r_1,\beta,-\delta) + G(r_1,\beta,0) + G(r_1,\beta,\delta) & 0.1 < x < 0.3, 0.1 < y < 0.3 \\ \max(1-10r_2, 0) & -0.3 < x < -0.1,\ 0.1 < y < 0.3 \\ F(r_3,\alpha,-\delta) + F(r_3,\alpha,0) + F(r_3,\alpha,\delta) & -0.3 < x < -0.1, -0.3 < y < -0.1 \\ 1 & 0.1 < x < 0.3, -0.3 < y < -0.1 \\ 0 & \text{otherwise} \end{cases}, \tag{20}$$

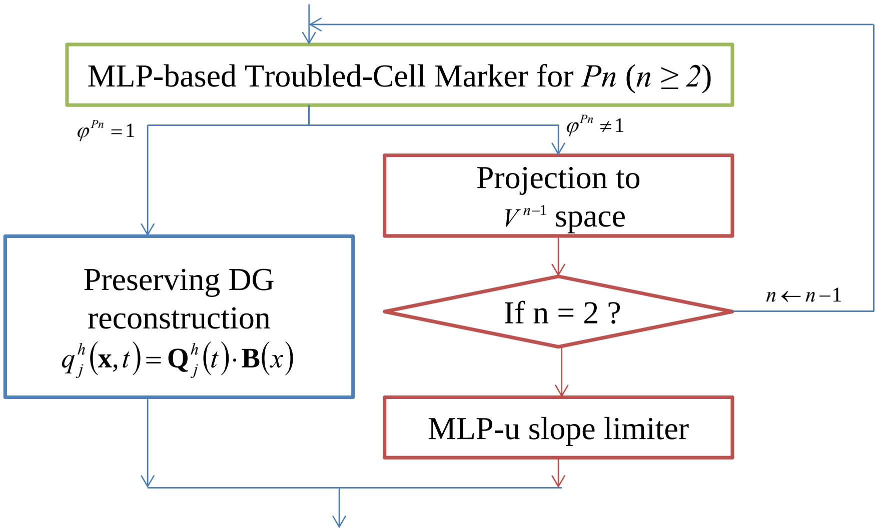

Figure 3: Flowchart of the hierarchical MLP method for DG-Pn reconstruction.

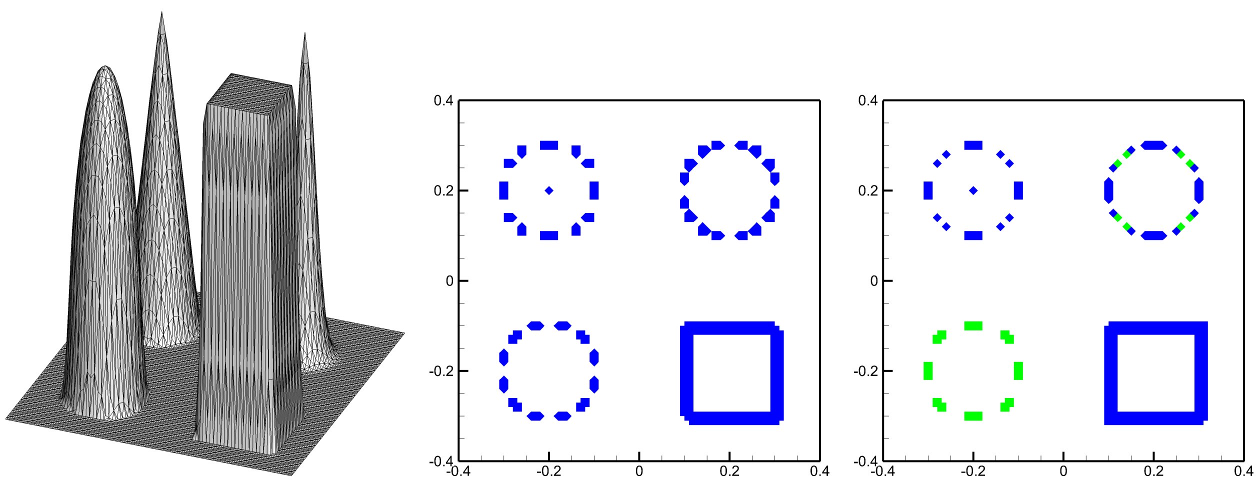

(a) Initial profiles (b) Hierarchical detector with DG-$P2$ (c) Hierarchical detector with DG-$P3$

Figure 4: Activation of limiter for various profiles. (Blue: Slope limiting, Green: Hierarchical limiting)

where $r_1 = |\mathbf{x} - (0.2, 0.2)|$, $r_2 = |\mathbf{x} - (-0.2, 0.2)|$ and $r_3 = |\mathbf{x} - (0.2, -0.2)|$. $G(x, \beta, x_c) = \exp(-\beta(x - x_c)^2)$ and $F(x, \alpha, x_c) = \sqrt{\max(1 - \alpha^2(x - x_c)^2, 0)}$ with $\beta = \log(2)/(360\delta^2)$, $\delta = 0.005$ and $\alpha = 10$. They represent a two-dimensional Gaussian hump, spike, half ellipsoid and cube at each quadrant.

Figure 4 shows the comparison of the activation region for DG-$P2$ and $P3$ reconstruction. The MLP troubled-cell markers accurately capture discontinuous jump along the cube boundary in fourth quadrant. Due to finite mesh size, the limiter is activated on a few cells along the boundary of hump, spike and ellipsoid. From the results, the MLP troubled-cell marker successfully distinguishes continuous region from discontinuous one in multi-dimensional flows.

4 Numerical Results

Extensive numerical experiments are carried out to assess the performance of the proposed limiting methods. Some well-known test problems for inviscid and viscous flow on 2-D triangular and 3-D tetrahedral grids are also examined up to the DG-$P3$ accuracy. The accuracy, robustness and efficiency characteristics of the hierarchical MLP methods are compared with the MLP-u slope limiters in FVM. All computations

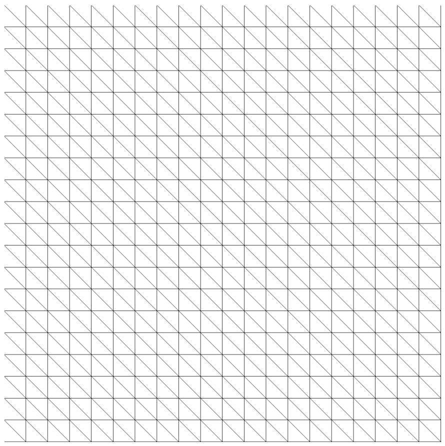

(a) Regular grid

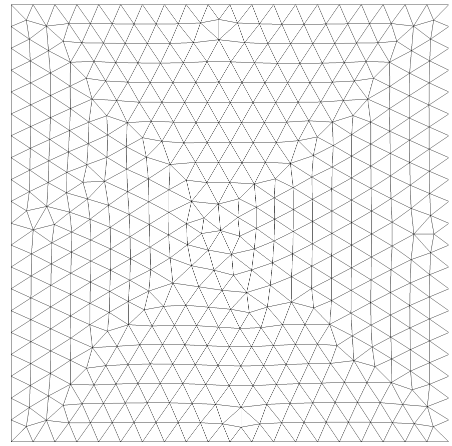

(b) Irregular grid

Figure 5: Regular and irregular triangular grids.

greater than DG-*P1* reconstruction employ the hierarchical MLP limiting algorithm, and the simple MLP-based troubled-cell marker with $K = 100$ is used for DG-*P1* reconstruction. As a numerical flux, local Lax-Friedrich scheme, RoeM [23] scheme and AUSMPW+ [24] scheme are adopted.

4.1 Convergence Studies

4.1.1 Euler Equations with an isentropic vortex advection

In order to examine numerical accuracy in multi-dimensional smooth flows without shock waves, inviscid flow with an isentropic vortex is considered. Since the flowfield is inviscid, the exact solution is just the passive advection of the initial vortex with a mean flow. The mean flow condition, which is considered as a free stream, is $\rho_\infty = 1, p_\infty = 1$ and $(u_\infty, v_\infty) = (1, 1)$. The perturbed values for the isentropic vortex are given by

$$(\delta u, \delta v) = \frac{\varepsilon}{2\pi} e^{0.5(1-r^2)(-\bar{y},\bar{x})}, \quad \delta T = -\frac{(\gamma-1)\varepsilon^2}{8\gamma\pi^2} e^{1-r^2}, \quad \delta S = 0. \tag{21}$$

The vortex strength is $\varepsilon = 5$. $(\bar{x}, \bar{y}) = (x - x_0, y - y_0)$, where (x_0, y_0) is the location of the vortex center, and $r^2 = \bar{x}^2 + \bar{y}^2$. Computational domain is $[-5, 5] \times [-5, 5]$, and periodic boundary condition is applied. RoeM scheme [23] is applied as a numerical flux. Figure 5 shows the regular and irregular grids used in grid refinement test. Tables 2 and 3 present the computed results, which clearly confirms the desired grid-convergence characteristic of the proposed limiting methods.

4.1.2 Navier-Stokes Equations with a Source Term

We also examine the grid convergence behavior of the proposed limiting for viscous flow with a source term. The reference analytic solution is a sinusoidal function and the source term can be derived by inserting it [20].

$$\begin{gathered}\mathbf{Q}_t + \nabla \cdot (\mathbf{F}_c - \mathbf{F}_v) = S, \\ \rho = e = \sin(\mathbf{k} \cdot \mathbf{x} - \omega t) + c, \mathbf{V} = \mathbf{1}.\end{gathered} \tag{22}$$

Following parameters are used.

$$Re = 2000, Pr = 0.72, \mathbf{k} = (\pi, \pi), \omega = \pi, c = 3.0. \tag{23}$$

Computational domain is $[0, 2] \times [0, 2]$, and periodic boundary condition is applied. Tables 4 and 5 shows that the proposed methods also maintain desired-accuracy for compressible Navier-Stokes equations.

Table 2: Grid refinement test for evolution of isentropic vortex on regular grids at $t = 10.0$.

	Grid	L^∞	Order	L^1	Order	L^2	Order
	20x20x2	4.8255E-02		2.9957E-03		7.1690E-03	
MLP-u1 on DG-*P1*	40x40x2	1.0472E-02	2.20	6.4309E-04	2.22	1.5355E-03	2.22
(K=100)	80x80x2	1.9421E-03	2.43	1.1591E-04	2.47	2.7089E-04	2.50
	160x160x2	3.9996E-04	2.28	2.2460E-05	2.37	5.2333E-05	2.37
	20x20x2	3.3952E-03		2.9147E-04		4.5641E-04	
Hierarchical	40x40x2	3.2963E-04	3.36	2.0734E-05	3.81	3.4920E-05	3.71
DG-*P2*-MLP	80x80x2	3.6873E-05	3.16	1.6946E-06	3.61	3.4730E-06	3.33
	160x160x2	4.3960E-06	3.07	1.6527E-07	3.36	3.9566E-07	3.13
	20x20x2	3.3145E-04		2.0910E-05		3.8876E-05	
Hierarchical	40x40x2	1.7153E-05	4.27	1.0618E-06	4.30	1.7078E-06	4.51
DG-*P3*-MLP	80x80x2	1.0891E-06	3.98	5.6998E-08	4.22	9.4731E-08	4.17
	160x160x2	6.1056E-08	4.16	3.5888E-09	3.99	6.5341E-09	3.86

Table 3: Grid refinement test for evolution of isentropic vortex on irregular grids at $t = 10.0$.

	Grid	L^∞	Order	L^1	Order	L^2	Order
	$h_0/20$	2.1201E-02		9.0050E-04		2.4341E-03	
MLP-u1 on DG-*P1*	$h_0/40$	3.9709E-03	2.42	1.9097E-04	2.24	5.3974E-04	2.17
(K=100)	$h_0/80$	1.1051E-03	1.85	4.1039E-05	2.22	1.2438E-04	2.12
	$h_0/160$	3.9996E-04	2.28	2.2460E-05	2.37	5.2333E-05	2.37
	$h_0/20$	1.5685E-03		1.0919E-04		2.0652E-04	
Hierarchical	$h_0/40$	2.0439E-04	2.94	9.7160E-06	3.49	1.9725E-05	3.39
DG-*P2*-MLP	$h_0/80$	2.4772E-05	3.04	9.0828E-07	3.42	2.0582E-06	3.26
	$h_0/160$	3.4006E-06	2.86	9.9905E-08	3.18	2.3472E-07	3.13
	$h_0/20$	1.1511E-04		9.3958E-06		1.5834E-05	
Hierarchical	$h_0/40$	8.4977E-06	3.76	5.3624E-07	4.13	9.5490E-07	4.05
DG-*P3*-MLP	$h_0/80$	8.9834E-07	3.24	2.5788E-08	4.38	5.0607E-08	4.24
	$h_0/160$	6.1718E-08	3.85	1.7351E-09	3.88	3.9565E-09	3.67

Table 4: Grid refinement test for 2-D Navier-Stokes equation on regular grids at $t = 1.0$.

	Grid	L^∞	Order	L^1	Order	L^2	Order
	20x20x2	2.0214E-02		8.7478E-03		5.3239E-03	
MLP-u1 on DG-*P1*	40x40x2	4.3511E-03	2.22	2.1461E-03	2.03	1.3032E-03	2.03
(K=100)	80x80x2	1.0267E-03	2.08	5.1602E-04	2.06	3.1455E-04	2.05
	160x160x2	2.5946E-04	1.98	1.2551E-04	2.04	7.5192E-05	2.06
	20x20x2	1.4214E-03		4.0574E-04		2.6083E-04	
Hierarchical	40x40x2	1.4308E-04	3.31	4.7896E-05	3.08	3.0922E-05	3.08
DG-*P2*-MLP	80x80x2	1.6937E-05	3.08	6.0937E-06	2.97	3.9690E-06	2.96
	160x160x2	2.0834E-06	3.02	7.8993E-07	2.95	5.1492E-07	2.95
	20x20x2	1.1441E-04		2.3764E-05		1.5897E-05	
Hierarchical	40x40x2	6.8429E-06	4.06	1.3973E-06	4.09	9.6450E-07	4.04
DG-*P3*-MLP	80x80x2	3.7134E-07	4.20	8.7247E-08	4.00	6.0400E-08	4.00
	160x160x2	1.7941E-08	4.37	5.5385E-09	3.98	3.7348E-09	4.02

Table 5: Grid refinement test for 2-D Navier-Stokes equation on irregular grids at $t = 1.0$.

	Grid	L^∞	Order	L^1	Order	L^2	Order
MLP-u1 on DG-*P1* (K=100)	$h_0/20$	2.2164E-02		4.8407E-03		3.1926E-03	
	$h_0/40$	5.8004E-03	1.93	1.1045E-03	2.13	7.5107E-04	2.09
	$h_0/80$	1.5192E-03	1.93	2.6095E-04	2.08	1.7732E-04	2.08
	$h_0/160$	3.4994E-04	2.13	6.3256E-05	2.05	4.2350E-05	2.07
Hierarchical DG-*P2*-MLP	$h_0/20$	7.1105E-04		1.3885E-04		8.9558E-05	
	$h_0/40$	8.8627E-05	3.00	1.5491E-05	3.16	1.0158E-05	3.14
	$h_0/80$	1.2532E-05	2.82	1.8569E-06	3.05	1.2175E-06	3.06
	$h_0/160$	1.3543E-06	3.22	2.3019E-07	3.02	1.4850E-07	3.05
Hierarchical DG-*P3*-MLP	$h_0/20$	2.5290E-05		4.9685E-06		3.2735E-06	
	$h_0/40$	1.6229E-06	3.96	2.5839E-07	4.26	1.7357E-07	4.24
	$h_0/80$	1.0403E-07	3.96	1.5684E-08	4.03	1.0753E-08	4.01
	$h_0/160$	8.4119E-09	3.64	1.0144E-09	3.96	7.1091E-10	3.93

Table 6: Grid refinement test for 3-D Navier-Stokes equation on irregular grids at $t = 0.25$.

	Grid	L^∞	Order	L^1	Order	L^2	Order
MLP-u1 on DG-*P1* (K=100)	16x16x16x6	6.1594E-02		1.0713E-02		1.4549E-02	
	24x24x24x6	2.2244E-02	2.51	4.6208E-03	2.07	6.2874E-03	2.07
	32x32x32x6	1.2685E-02	1.95	2.4957E-03	2.14	3.4134E-03	2.12
	48x48x48x6	5.9274E-03	1.88	1.0459E-03	2.15	1.4468E-03	2.12
Hierarchical DG-*P2*-MLP	16x16x16x6	4.0047E-03		8.4467E-04		1.1538E-03	
	24x24x24x6	1.4091E-03	2.58	2.5119E-04	2.99	3.5286E-04	2.92
	32x32x32x6	5.9899E-04	2.97	1.0301E-04	3.10	1.5035E-04	2.97
	48x48x48x6	1.7286E-04	3.07	2.9471E-05	3.09	4.3871E-05	3.04
Hierarchical DG-*P3*-MLP	16x16x16x6	9.9175E-04		7.6044E-05		1.1026E-04	
	24x24x24x6	1.5784E-04	4.53	1.4438E-05	4.10	2.1022E-05	4.09
	32x32x32x6	4.9437E-05	4.04	4.3510E-06	4.17	6.4505E-06	4.11
	48x48x48x6	1.0382E-05	3.85	8.0788E-07	4.15	1.2166E-06	4.11

The grid-convergence behavior of the hierarchical MLP schemes on 3-D tetrahedral grids is examined by solving a 3-D Navier-Stokes problem. The spatial parameter $\mathbf{k}$ is (π, π, π) and other conditions are the same as before. Computational domain is $[0, 2] \times [0, 2] \times [0, 2]$ with periodic boundary condition, and tetrahedral elements are created by dividing a cube along diagonals.

Table 6 shows the quantitative comparison of solution errors at $t = 0.25$. Similar to the grid-convergence behavior observed on 2-D triangular grids, the proposed methods successfully maintains the desired accuracy, especially around local extrema.

4.2 A Mach 3 wind tunnel with a step

As one of standard test cases to examine high-resolution schemes. we consider a uniform Mach 3 flow in wind tunnel with a step, whose size is 3 length unit long and 1 length unit high. The step is 0.2 length unit high, located at 0.6 length unit from the left end of the tunnel. Reflective boundary condition is applied along the wall, and in-flow free stream and out-flow extrapolation conditions are applied at the entrance and exit. Around the expansion corner, computational meshes are slightly clustered without any special treatment, as in Ref. [4]. Local Lax-Friedrich scheme is applied as a numerical flux.

Figure 6 shows the density contours computed on triangular grids of $h = 1/160$ at $t = 4.0$. Similar to the previous test case, one can check the resolving capability of the DG-MLP methods for the shear layer instability from the shock triple point as the order of DG reconstruction increases from *P1* to *P3*.

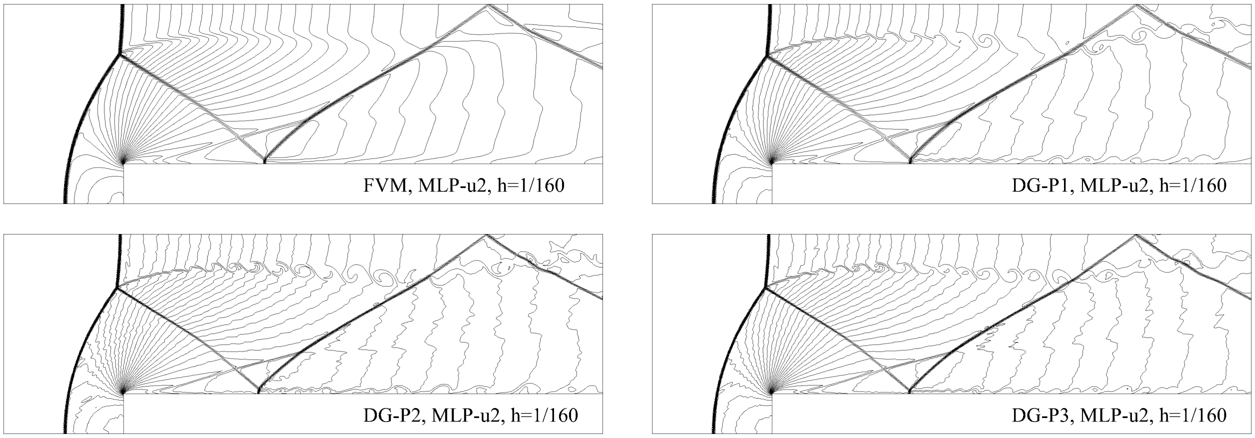

Figure 6: Comparison of density contours for the Mach 3 wind tunnel with a step.

4.3 Interaction of shock wave with spherical density bubble

The unsteady flow physics of shock-bubble interaction has been extensively studied since it can provide a numerical benchmark of vorticity and turbulence generation in compressible flows [25]. The baroclinic torque, caused by the density gradient normal to spherical bubble surface and the pressure gradient by a moving shock, develops a 3-D vortex structure behind the moving shock. Exploiting the flow symmetry, computational domain is a quadrant of shock tube with the interval of $[0, 13.35]$ in the x-direction and $[0, 4.45] \times [0, 4.45]$ in the y-z plane. Initially, the quarter of spherical bubble with $r = 2.5$ is placed at $x = 3.5$, and the moving shock with $M_s = 3.0$ is located at $x = 0.5$. Grid system consists of 8.90 million tetrahedral elements. With Tachyon 2 supercomputer at KISTI, MPI parallel computation was performed with 1024 CPUs to reach at $t = 3.5$, and RoeM flux is used.

Figures 7 and 8 shows the three-dimensional density contours by DG-*P3* with the MLP limiting. Similar to the two-dimensional case, the primary and secondary vortex structure, the tail vortical structure after the primary vortex, and the 3-D monotonic shock are well captured.

4.4 Two-dimensional Richtmyer-Meshkov Instability

Richtmyer-Meshkov instability accompanies complex flow structure by interacting shock wave and interface of different gas density. In particular, misalignment of density and pressure gradients generates a baroclinic vortex structure. This flow structure can be analyzed for inviscid and viscous cases, and high Reyonolds number case provide chaotic flow structure by flow instability [26]. The present computation solves compressible viscous flow with $Re = 10^5$. Computational domain is $[-2, 6] \times [0, 1]$, and the initial condition of a moving shock with $M_s = 2$ and density difference is imposed as follows.

$$
\begin{aligned}
(\rho_1, u_1, v_1, p_1) &= (2.667, 1.479, 0.0, 4.5) \text{ if } \; x < -0.2, \\
(\rho_2, u_2, v_2, p_2) &= (1.0, 0.0, 0, 1.0) \text{ if } \; x \geq -0.2, \; x < y, \\
(\rho_3, u_3, v_3, p_3) &= (3.0, 0.0, 0, 1.0) \text{ if } \; x \geq -0.2, \; x \geq y.
\end{aligned} \tag{24}
$$

Grid system consists of triangular elements whose characteristic lengths are $h = 1/100, 1/200$. Figures 9 and 10 compare density contours at $t = 3.3$. Similar to the previous test cases, the hierarchical MLP algorithm provides a sufficient resolution to capture complex vortex structure while the result obtained by the second-order FVM-MLP is relatively smeared out by numerical dissipation.

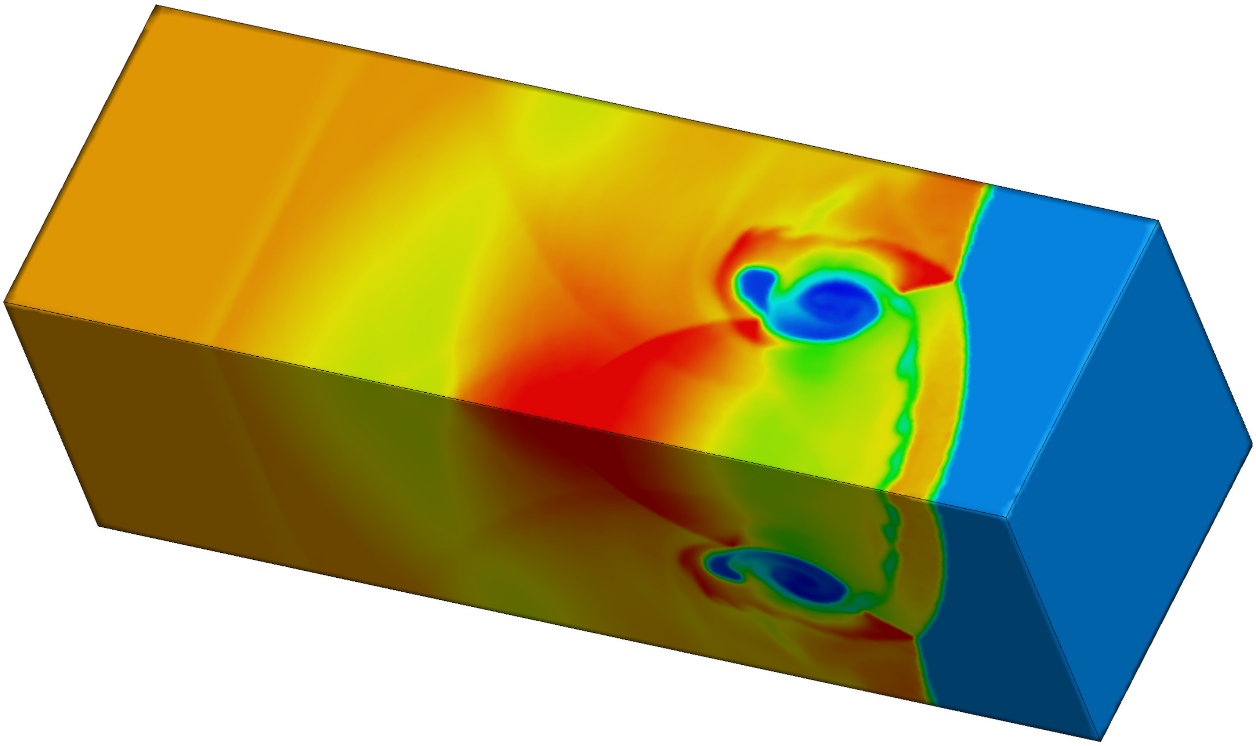

Figure 7: Density contours of interaction of 3-D density bubble with shock wave at $t = 3.5$.

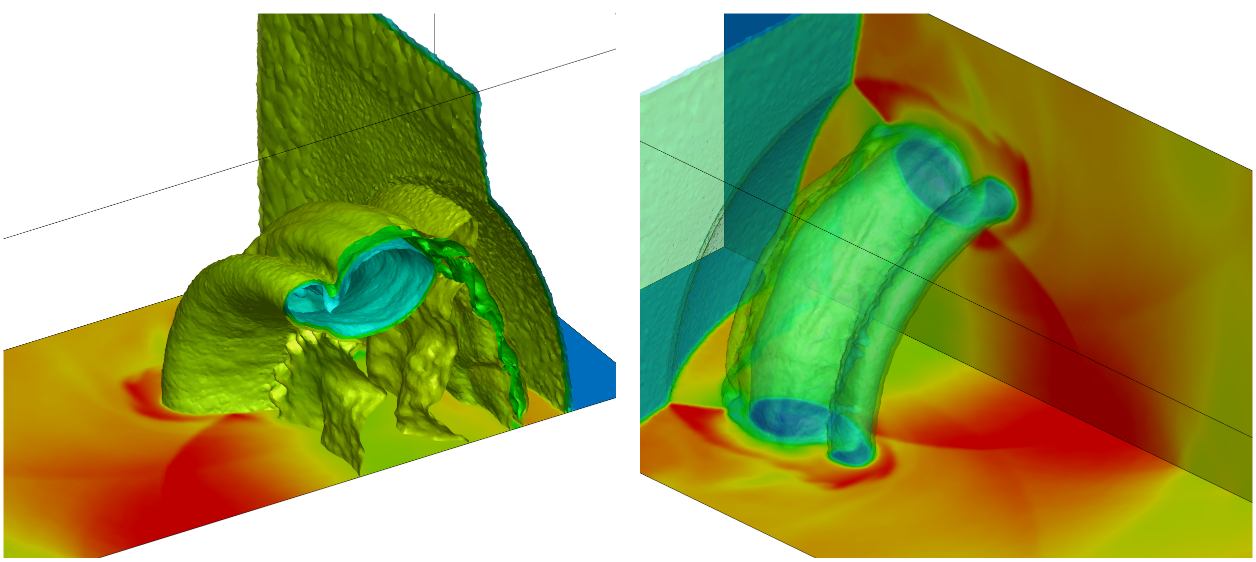

Figure 8: Close-up view around vortex torus at $t = 3.5$.

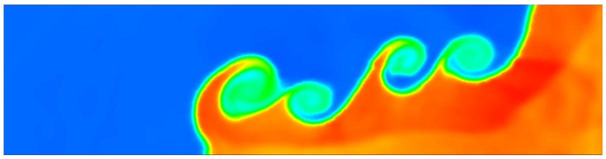

(a) FVM

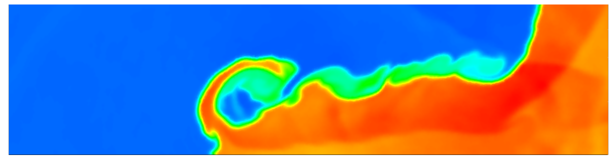

(b) DG-*P1*

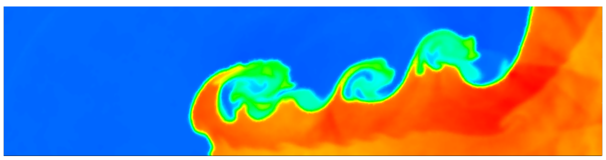

(c) DG-*P2*

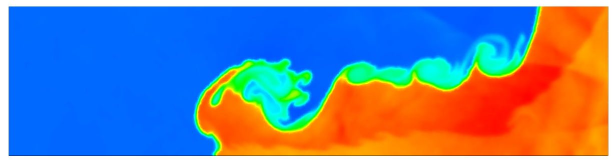

(d) DG-*P3*

Figure 9: Comparison of density contours for Richtmyer-Meshkov instability on coarse grids.

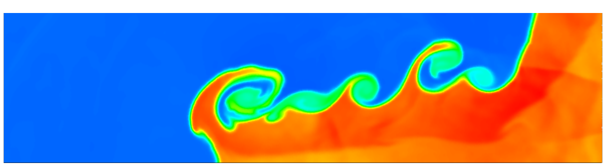

(a) FVM

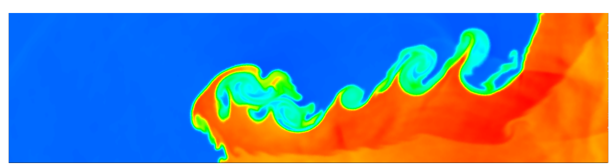

(b) DG-*P1*

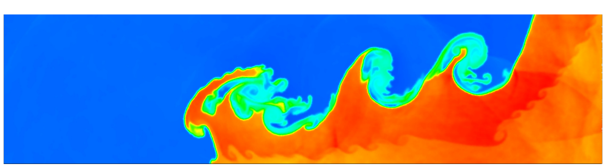

(c) DG-*P2*

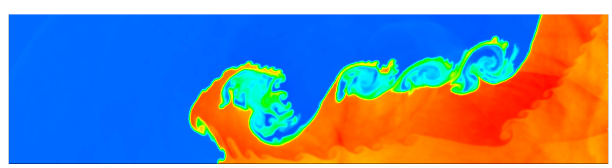

(d) DG-*P3*

Figure 10: Comparison of density contours for Richtmyer-Meshkov instability on fine grids.

4.5 Oblique Shock-Mixing Layer Interaction

4.5.1 Two-dimensional Case

This test is to assess the performance of capturing small scale vortical structure interacting with shock discontinuity [27]. A spatially developing mixing layer produces a series of vortices, and the oblique shock originating from the upper-left corner impinges on the mixing layer. This oblique shock is deflected by the shear layer and then reflects again from the bottom slip wall, which leads to the interaction between downstream vortices and the reflected shock.

For the initial condition, hyperbolic tangent velocity profile and convective Mach number are imposed.

$$u = 2.5 + 0.5\tanh(2y), \tag{25}$$

$$M_c = \frac{u_1 - u_2}{c_1 - c_2} = 0.6. \tag{26}$$

The upper boundary condition is specified to satisfy the oblique shock with $\beta = 12°$, and the lower boundary condition is slip wall. Fluctuation adding to the mean in-flow is given by

$$v' = \sum_{k=1}^{2} a_k \cos(2\pi kt/T + \phi_k)\exp(-y^2/b), \tag{27}$$

with the period $T = \lambda/u_c$, wavelength $\lambda = 30$ and convective velocity $u_c = 2.68$. Other parameters are $a_1 = a_2 = 0.05$, $\phi_1 = 0$, $\phi = \pi/2$ and $b = 10$. Reynolds number and Prandtl number are 500 and 0.72, respectively. Computational domain is $[0, 200] \times [-20, 20]$. While many filter methods solve this problem with stretched grids in the y-direction for better resolution, the present computation applies the uniformly distributed triangular grids of $h = 0.75, 0.5$.

Figures 11 and 12 show the comparison of pressure contours by the FVM-MLP and DG-MLP methods at $t = 120$. While the vortex structure by the second-order FVM-MLP on coarse grid are almost smeared out, the higher-order DG-MLP reconstructions resolve the vortical structure more clearly. The result of FVM on fine grid is almost similar to the result of the DG-*P1*-MLP on coarse grid. The DG-*P3*-MLP on fine grids provides detailed flow structure, especially downstream shock-vortex interaction.

4.5.2 Three-dimensional Case

The previous test case can be extended into three-dimensional space. Computational domain is the extrusion of the two-dimensional surface along the z-direction, and symmetric boundary condition is imposed at both ends. In order to examine three-dimensional effect, the inflow condition is modified as follows.

$$v' = \sum_{k=1}^{2} a_k \cos(2\pi kt/T + z/L_z + \phi_k)\exp(-y^2/b), \tag{28}$$

where L_z, the extrusion length, is 40. Grid system consists of 7.7 million tetrahedral elements. With Tachyon 2 supercomputer at KISTI, MPI parallel computation was performed with 1024 CPUs to reach at $t = 120$.

Figure 13 shows the density contour and iso-surfaces at $t = 120$. Due to the three-dimensional perturbation (Eq. (28)), phase difference is induced along the z-direction. Figure 14 shows the slice of the density contour at various x positions. Before the oblique shock strikes the mixing layer (at $x = 85$), spanwise vortical structure is regularly developed along the z-direction. At $x = 150$, spanwise vortical structure is noticeably deformed after the oblique shock-mixing layer interaction. After the reflected shock hits the mixing layer again, compressive waves are developed and the spanwise shock-vortex interaction is further developed. Figure 15 shows the density and pressure contours at $z = -10, 10$ planes. The phase difference along the z-direction is clearly observed.

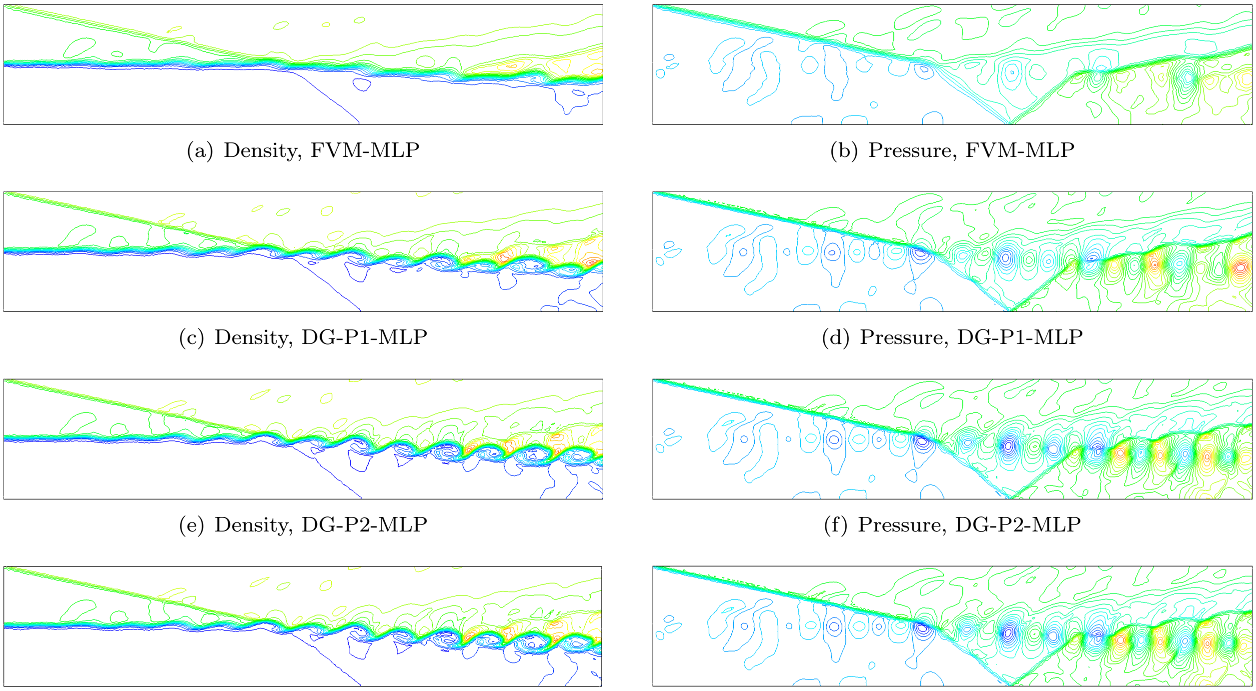

(a) Density, FVM-MLP
(b) Pressure, FVM-MLP
(c) Density, DG-P1-MLP
(d) Pressure, DG-P1-MLP
(e) Density, DG-P2-MLP
(f) Pressure, DG-P2-MLP
(g) Density, DG-P3-MLP
(h) Pressure, DG-P3-MLP

Figure 11: Comparison of pressure contours of shock-mixing layer interaction on coarse grids

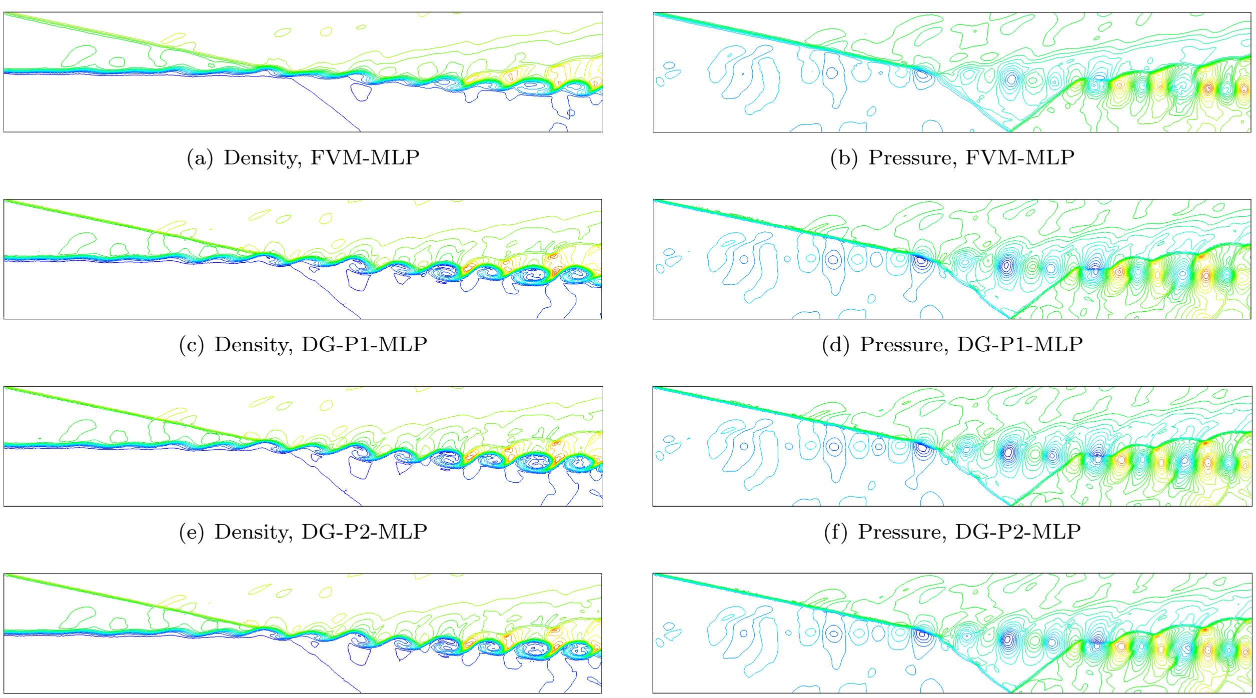

(a) Density, FVM-MLP
(b) Pressure, FVM-MLP
(c) Density, DG-P1-MLP
(d) Pressure, DG-P1-MLP
(e) Density, DG-P2-MLP
(f) Pressure, DG-P2-MLP
(g) Density, DG-P3-MLP
(h) Pressure, DG-P3-MLP

Figure 12: Comparison of pressure contours of shock-mixing layer interaction on fine grids

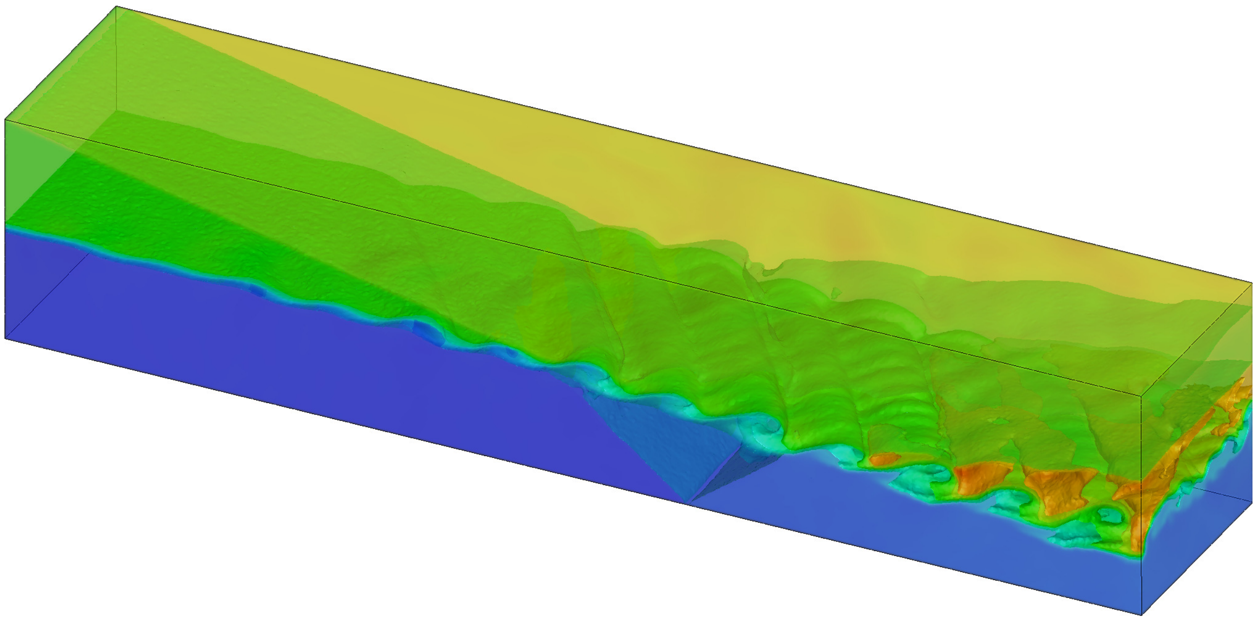

Figure 13: Density contours of three dimensional oblique shock-mixing layer interaction at $t = 120$.

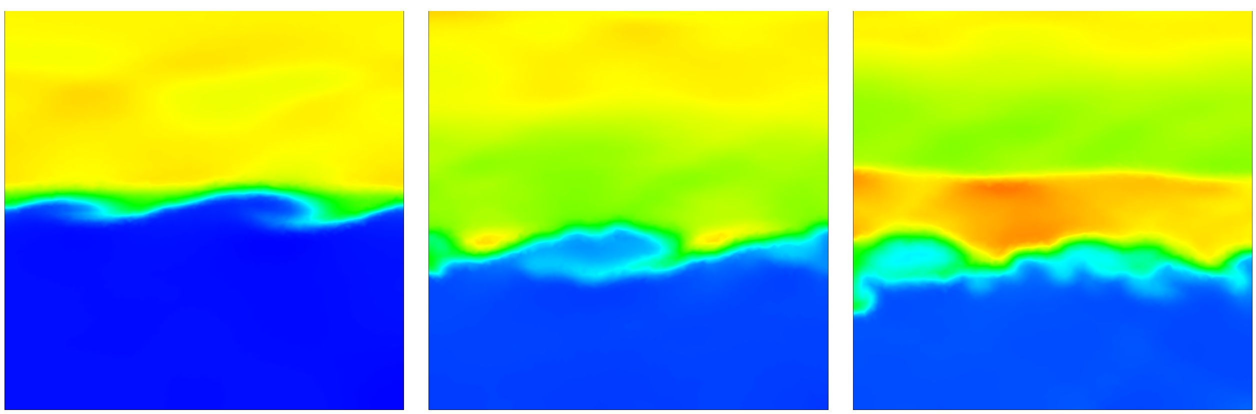

(a) $x = 85$ (b) $x = 150$ (c) $x = 190$

Figure 14: Spanwise density distributions at x=85, 150, 190 positions

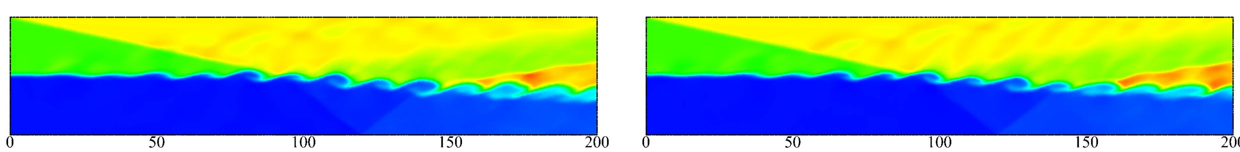

(a) $z = -10$, Density (b) $z = 10$, Density

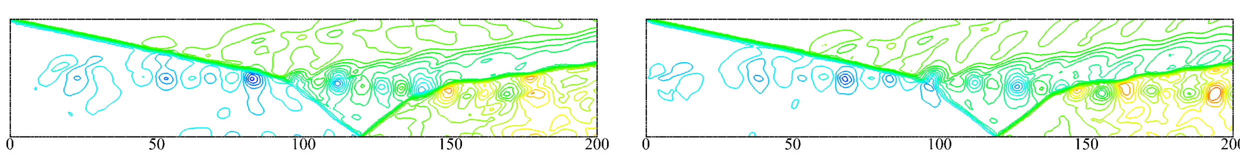

(c) $z = -10$, Pressure (d) $z = 10$, Pressure

Figure 15: Streamwise density and pressure distributions at z=-10, 10 positions

5 Conclusion

The hierarchical MLP limiting strategy for arbitrary higher-order DG reconstruction is able to capture complex multi-dimensional flow structures without yielding unwanted oscillations for compressible flows. Guided by the MLP condition and the maximum principle, the multi-dimensional limiting process is successfully extended into the DG framework. Combined the augmented MLP condition with a simple extrema detector, an efficient and accurate troubled-cell marker is proposed up to DG-$P2$ reconstruction. Furthermore, by examining the behavior of local extrema, the uncertainty of determining a parameter for slope limiting is eliminated, which leads to the formulation of the hierarchical MLP method for Pn ($n \geq 2$). By employing the BR2 scheme to handle the diffusion term, the proposed approach can accurately resolve compressible viscous flows. Extensive numerical experiments for inviscid and viscous flows verifies that the proposed limiting provides detailed multi-dimensional flow structures without yielding oscillations in both continuous and discontinuous region.

Acknowledgments

Authors appreciate the financial supports provided by NSL (National Space Lab.) program through the National Research Foundation of Korea funded by the Ministry of Education, Science and Technology (Grant 20110029871), by National Institute for Mathematical Sciences (NIMS) grant funded by the Korea government (No. A21001) and by the Ministry of Land, Transport and Maritime Affairs (MLTM) through the Super Long Span Bridge R&D Center in Korea. This work is also supported by the KISTI Supercomputing Center (KSC-2010-C1-0031) and by PLSI supercomputing resources of KISTI.

References

[1] Bernardo Cockburn, George Karniadakis, and Chi-Wang Shu. *Discontinuous Galerkin methods: theory, computation, and applications*, volume 11 of *Lecture Notes in Computational Science and Engineering*. Springer-Verlag Inc., pub-SV:adr, 2000.

[2] Zhi Jian Wang. High-order methods for the Euler and Navier-Stokes equations on unstructured grids. *Progress in Aerospace Sciences*, 43(1-3):1 – 41, 2007.

[3] Zhi Jian Wang. *Adaptive High-Order Methods in Computational Fluid Dynamics*, volume 2. World Scientific Pub Co Inc, 2011.

[4] Bernardo Cockburn and Chi-Wang Shu. The Runge-Kutta discontinuous Galerkin method for conservationlaws V: multidimensional systems. *Journal of Computational Physics*, 141(2):199 – 224, 1998.

[5] Rupak Biswas, Karen D. Devine, and Joseph E. Flaherty. Parallel, adaptive finite element methods for conservation laws. *Applied Numerical Mathematics*, 14(1-3):255–283, 1994.

[6] Anne Burbeau, Pierre Sagaut, and Charles Henri Bruneau. A problem-independent limiter for high-order Runge-Kutta discontinuous Galerkin methods. *Journal of Computational Physics*, 169(1):111 – 150, 2001.

[7] Michael Yang and Zhi Jian Wang. A parameter-free generalized moment limiter for high-order methods on unstructured grids. In *47 th AIAA Aerospace Sciences Meeting Including the New Horizons Forum and Aerospace Exposition*, number AIAA 2009-605. American Institute of Aeronautics and Astronautics, 2009.

[8] Zhiliang Xu, Yingjie Liu, and Chi-Wang Shu. Hierarchical reconstruction for discontinuous Galerkin methods on unstructured grids with a WENO-type linear reconstruction and partial neighboring cells. *Journal of Computational Physics*, 228(6):2194 – 2212, 2009.

[9] Zhiliang Xu, Yingjie Liu, Huijing Du, Guang Lin, and Chi-Wang Shu. Point-wise hierarchical reconstruction for discontinuous Galerkin and finite volume methods for solving conservation laws. *Journal of Computational Physics*, 230(17):6843 – 6865, 2011.

[10] Jun Zhu, Jianxian Qiu, Chi-Wang Shu, and Michael Dumbser. Runge-Kutta discontinuous Galerkin method using WENO limiters II: unstructured meshes. *Journal of Computational Physics*, 227(9):4330 – 4353, 2008.

[11] Hong Luo, Joseph D. Baum, and Rainald Löner. A discontinuous Galerkin method based on a Taylor basis for the compressible flows on arbitrary grids. *Journal of Computational Physics*, 227(20):8875 – 8893, 2008.

[12] Jun Zhu and Jianxian Qiu. Hermite WENO schemes and their application as limiters for Runge-Kutta discontinuous Galerkin method, III: unstructured meshes. *Journal of Scientific Computing*, 39(2):293–321, 2009.

[13] Kyu Hong Kim and Chongam Kim. Accurate, efficient and monotonic numerical methods for multi-dimensional compressible flows: Part II: multi-dimensional limiting process. *Journal of Computational Physics*, 208(2):570 – 615, 2005.

[14] Jin Seok Park, Sung-Hwan Yoon, and Chongam Kim. Multi-dimensional limiting process for hyperbolic conservation laws on unstructured grids. *Journal of Computational Physics*, 229(3):788 – 812, 2010.

[15] Jin Seok Park and Chongam Kim. Multi-dimensional limiting process for finite volume methods on unstructured grids. *Computers and Fluids*, In press, 2012.

[16] Jin Seok Park and Chongam Kim. Multi-dimensional limiting process for discontinuous Galerkin methods on unstructured grids. In *Computational Fluid Dynamics 2010: Proceedings of the Sixth International Conference on Computational Fluid Dynamics, ICCFD6, St Petersburg, Russia, on July 12-16 2010*, pages 179 – 184. Springer Verlag, 2011.

[17] Jin Seok Park and Chongam Kim. Arbitrary higher-order multi-dimensional limiting strategies for discontinuous Galerkin methods on unstructured grids. *Journal of Computational Physics*, submittted.

[18] Francesco Bassi, Andrea Crivellini, Stefano Rebay, and Marco Savini. Discontinuous Galerkin solution of the Reynolds-averaged Navier-Stokes and $k - \omega$ turbulence model equations. *Computers & Fluids*, 34:507 – 540, 2005.

[19] Raymond J. Spiteri and Steven J. Ruuth. A new class of optimal high-order strong-stability-preserving time discretization methods. *SIAM Journal on Numerical Analysis*, 40:469–491, 2001.

[20] Gregor J. Gassner., Frieder Lörcher, and Claus Dieter Dieter Munz. A discontinuous Galerkin scheme based on a space-time expansion ii. viscous flow equations in multi dimensions. *Journal of Scientific Computing*, 34:260–286, 2008. 10.1007/s10915-007-9169-1.

[21] Michael Dumbser. Arbitrary high order PNPM schemes on unstructured meshes for the compressible Navier-Stokes equations. *Computers & Fluids*, 39(1):60 – 76, 2010.

[22] Lilia Krivodonova, Jianguo Xin, Jean Francois Remacle, Nicolas Chevaugeon, and Joseph E. Flaherty. Shock detection and limiting with discontinuous galerkin methods for hyperbolic conservation laws. *Applied Numerical Mathematics*, 48(3-4):323–338, 2004.

[23] Sung-Soo Kim Kim, Chongam Kim, Oh-Hyun Rho, and Seung Kyu Hong. Cures for the shock instability: development of a shock-stable Roe scheme. *Journal of Computational Physics*, 185(2):342 – 374, 2003.

[24] Kyu Hong Kim, Chongam Kim, and Oh-Hyun Rho. Methods for the accurate computations of hypersonic flows: I. AUSMPW+ scheme. *Journal of Computational Physics*, 174(1):38 – 80, 2001.

[25] A. Bagabir and Dimitris Drikakis. Mach number effects on shock-bubble interaction. *Shock Waves*, 11(3):209–218, 2001.

[26] Helen C. Yee and Björn Sjögreen. Simulation of Richtmyer–Meshkov instability by sixth-order filter methods. *Shock Waves*, 17(3):185–193, 2007.

[27] Helen C. Yee, Neil D. Sandham, and M. Jahed Djomehri. Low-dissipative high-order shock-capturing methods using characteristic-based filters. *Journal of Computational Physics*, 150(1):199 – 238, 1999.